Direct Observation of Bulk Second Harmonic Generation inside a Glass Slide with Tightly Focused Optical Fields

Xianghui Wang,[1,2] Shima Fardad,[1] Susobhan Das,[1] Alessandro Salandrino,[1] and Rongqing Hui[1,*]

[1]*Department Electrical Engineering & Computer Science, University of Kansas, Lawrence, KS, 66045, USA*
[2]*Institute of Modern Optics, Nankai University, Key Laboratory of Optical Information Science and Technology, Ministry of Education, Tianjin, 300071, China*

Correspondence and requests for materials to: rhui@ku.edu

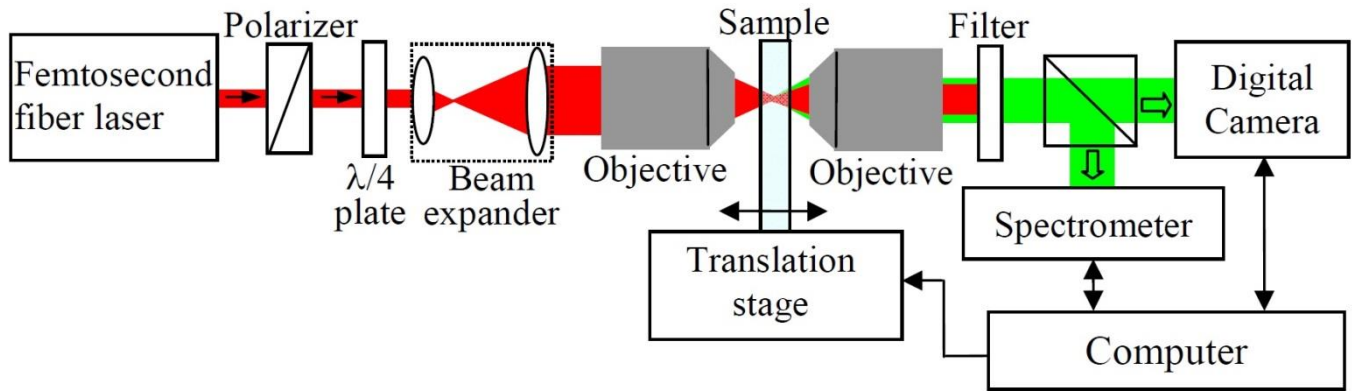Contents:

1. Experimental setup

Fig. S1. Schematic of the experimental setup.

2. Spectra

After the fundamental beam was removed by a short-pass filter, the spectra of both THG and SHG could be measured by the spectrometer. Fig. S2 shows typical spectra of THG and SHG. Note that the leaked-through fundamental beam at 1075nm wavelength can still be seen. While the strongest THG was obtained when the excitation focal position was at the surface, the SHG spectra were measured inside the bulk of the glass slide.
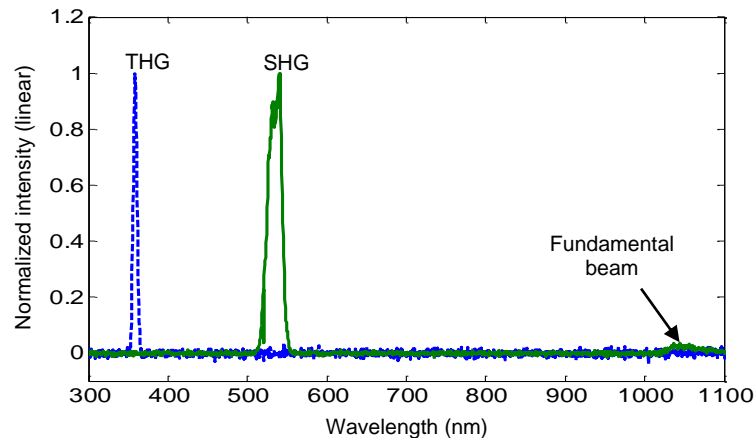

Fig. S2. Measured spectra of THG (blue dashed line) and SHG (green solid line) in a borosilicate glass slide.

3. Z-scan measurements of other types of glass slides

Fig. S3 shows an example of normalized SH and TH power as the function of excitation beam focal position in a z-scan measurement of BK7 glass slides with the thickness of 930μm. The glass thickness T_G was determined from the sample translation distance Δz between the two peaks of the THG spectrum as $T_G = n\Delta z$, where n is the linear refractive index of the glass. The Δz values measured for the borosilicate glass sample (Fig.2) and the BK7 glass sample (Fig.S3) are 97μm and

617μm, respectively. Because the refractive index of $n = 1.507$ for both of them at 1075nm excitation wavelength, their thicknesses are 146μm and 930μm, respectively.

The SHG efficiency increases with the focal position scanning further into the sample. In fact, the maximum SH intensity in the BK7 was obtained at approximately 672μm from the front surface, and this maximum SH intensity is 70 times higher than that measured at 137μm from the front surface where the maximum SH in the thin borosilicate glass was obtained. In order to make fair comparison for glass samples with different thickness, we used SH power levels measured when the focal position was 137μm from the front surface for all the samples in the calculation of power conversion efficiency shown in Fig. 3.
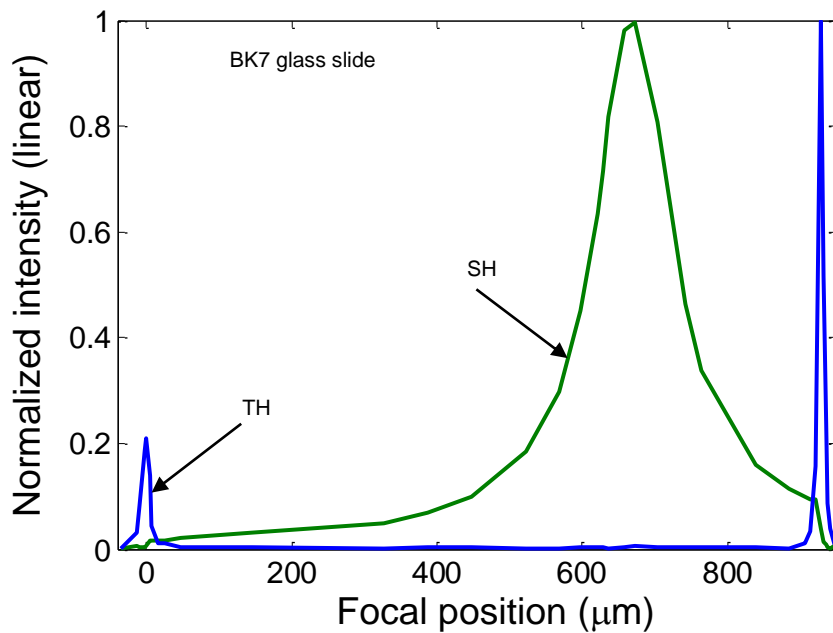

Fig. S3. SH (green) and TH (blue) intensities measured from a 930 μm BK7 glass slide by scanning the excitation focal position (z-scan).

Fig. 2 in the paper shows that for a thin glass slide (146μm borosilicate) the maximum SHG was obtained when the excitation focal position was near the second surface. Whereas Fig.S3 shows that for the thicker glass slide (930μm BK7), the maximum SHG was obtained further away (~258μm) from the second surface where the spot of the excitation beam reached the minimum size. This is believed to be caused by the limitation of the glass thickness correction of the focusing objective, which is specified as between 0 to 0.7mm [20].

In a similar experimental setup, a mode-locked Ti:sapphire laser (Mai Tai BB, Spectra Physics) is used with 790nm wavelength and approximately 80 fs pulse width at a repetition rate of 80 MHz. The incident beam is focused by an infinity-corrected dry objective (CFI_Plan_Apo_Lambda, 40X,

NA=0.95, Nikon) with adjustable cover glass correction capability ranging from 110μm to 230μm. SH signal is collected by another objective (CFI_TU_Plan_Fluor_EPI, 100X, NA=0.9, Nikon) with a long working distance of 1.0mm. The sample is a N-BK7 window (Edmund optics) with a thickness of 200μm. Photodetection is performed by a highly sensitive cooled photomultiplier tube (H7422-01, Hamamatsu), and the fundamental beam is chopped at 100 Hz in order to be detected through a lock-in amplifier so that background noise can be removed. The scattered fundamental photons are removed by several band-pass filters placed before the photomultiplier tube.
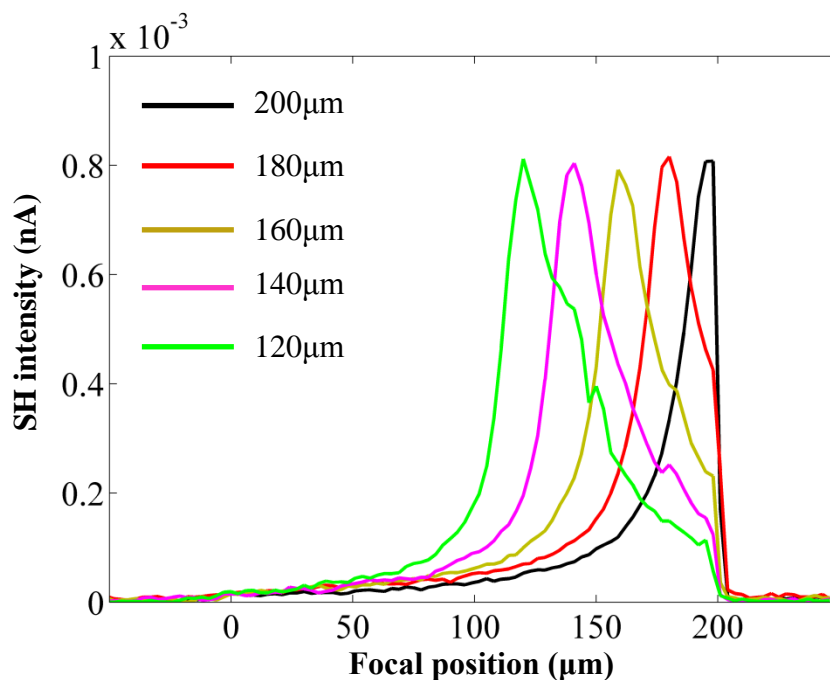

Fig. S4 Intensities of SHG as the function of focal position inside a N-BK7 glass slide with a thickness of 200μm for different settings of cover glass correction.

Fig. S4 shows results from z-scan measurements of SH signal at different settings of cover glass correction in the objective. As the cover glass correction thickness is adjusted from 120μm to 200μm, the location of the maximum SHG is moved accordingly toward the second surface. For different cover glass correction, the maxima almost have the same magnitude. Therefore, dynamic aberration correction of the focusing objective plays a key role in the increase of SHG when the focal point is moved deep into the sample.

With a fixed setting of cover glass correction of the objective at a thickness 110μm, SH intensity as the function of excitation focal position is measured for different pump powers, and the results are shown in Fig.S5. There is no noticeable variation in the SH signal peak position when the pump power increases from 100mW to 150mW. Instead, the SH signal peak position at approximately

110μm from the first surface of the glass is primarily determined by the setting of the cover glass correction of the objective.
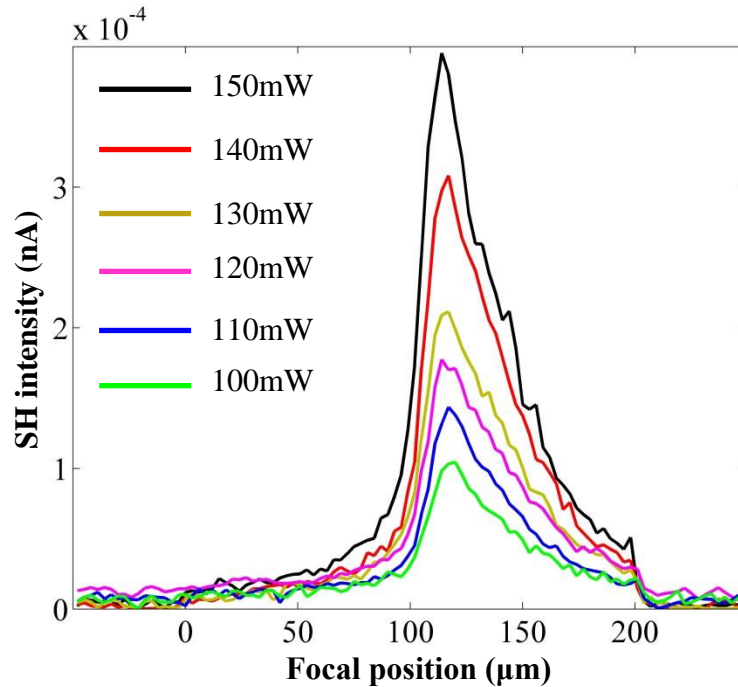

Fig. S5. SH intensity as the function of focal position for different pump power levels. The glass thickness correction of objective is fixed at 110μm.

4. Dependence of SH peak amplitude on pump power

In the first experimental setup, the optical power of the SH was measured by a TE cooled silicon photodetector (S-010-TE2-H receiver module, Electro-optical Systems Inc.) with a noise equivalent power of 10^{-14} W/√Hz. The responsivity of this TE cooled detector was calibrated against a standard optical power meter at 555nm wavelength, and the linearity was checked against a set of optical attenuators. Transmission losses of collecting objective and short-pass and bandpass filters were subtracted from the power measurement.

The conversion efficiency is defined as the power ratio between the generated SH component and the excitation beam at the fundamental frequency. Fig.S6 shows the SH power measured 20μm from the front surface (open squares), at the middle of the sample (open triangles), and 137μm from the front surface (open circles) as the function of the pump power in dBW. The slopes of the output/input power relation are 3.44dB/dB, 3.57dB/dB, and 3.84dB/dB, respectively. These slopes are clearly much higher than the expected value of 2 for the square-law characteristic of SHG. This indicates that self-focusing due to Kerr effect nonlinearity in the glass must have been involved, which brings the slope of output/input power relation close to quadrature dependence. Because of the nonlinear nature

of SHG, which is evident from Fig.S6, the conversion efficiency is also pump power-dependent. In our measurement with the borosilicate glass sample, the power conversion efficiency is approximately -51.2dB (corresponding to 7.6×10^{-6} in linear scale) at 0dBW (1W in linear scale) pump power. Note that the power conversion efficiencies reported in Fig. 3 were obtained with 0.5W pump power for all samples, and the focal point of the excitation beam was positioned at 137μm from the front surface for fair comparison. However, much higher (~70 times) conversion efficiencies could be obtained for thicker glasses when the focal position was placed deeper inside the sample as illustrated in Fig.S3.
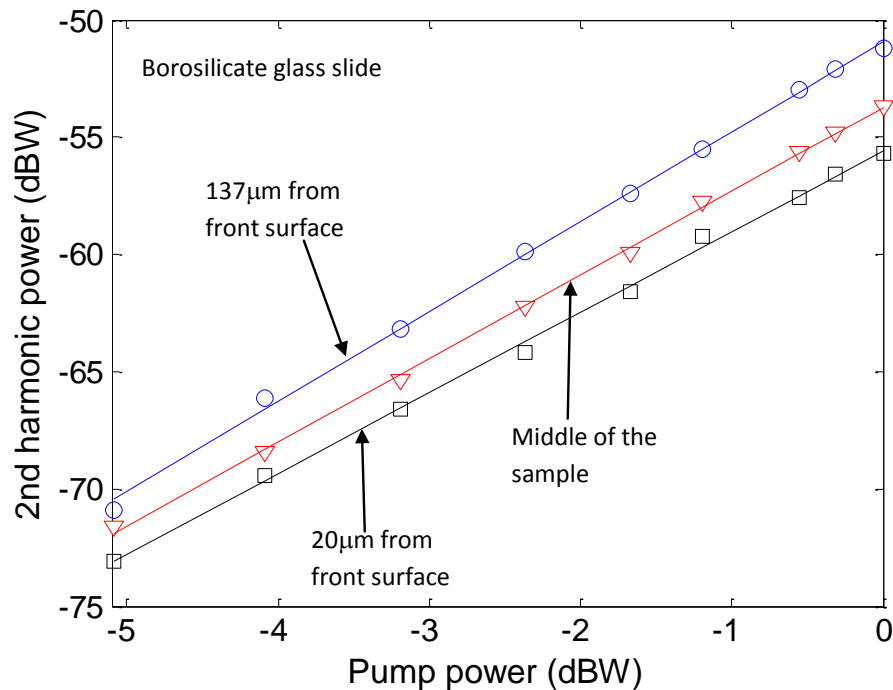

Fig. S6. Bulk SH power inside borosilicate glass slide as a function of the fundamental beam power measured with different focal positions inside the sample.

The experimental setup used to obtain Fig.S4 and Fig.S5 was also used to test the intensities of SH signal as the function of the fundamental pump power in a relatively low power regime, and the results are shown in Fig.S7. Fig.S7(a) shows that in the range of pump power between 10mW and 60 mW, the dependence of SH signal on pump power is almost quadratic with a slope of 2.23dB/dB. However, as the pump power increases to the region between 100mW and 195mW, this slope is increased to 3.44dB/dB as shown in Fig. S7(b). This slope increase with the increase of pump power is attributed to the effect of self-focusing.
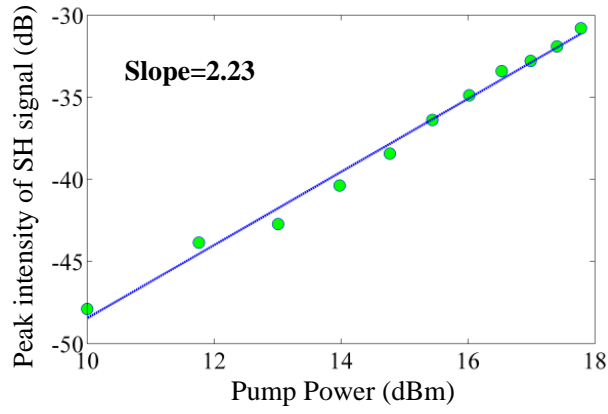
(a)
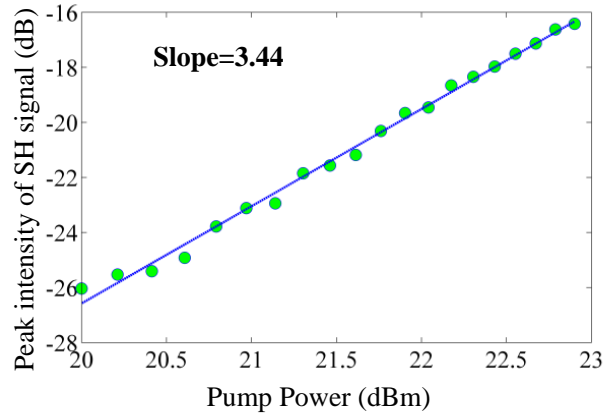
(b)

Fig. S7. Intensities of SHG as the function of pump power when glass thickness correction is fixed at 110μm.

5. Theoretical model of bulk SHG inside centrosymmetric material under tightly focused excitation

As shown in Fig. S8, an incoming plane wave (PW) at the fundamental frequency ω propagates along the z axis and is focused by an infinity-corrected objective inside a glass slide. The origin O of the Cartesian coordinate system is defined as the focal point of the excitation beam, and $\mathbf{r}$ is the position vector in the focal region. α is the maximal beam angle determined by the NA of the focusing objective.
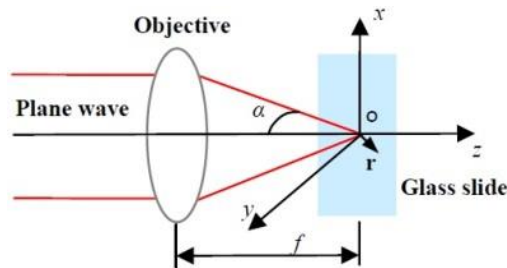

Fig. S8 Schematic diagram of a PW focused by an infinity-corrected objective inside a glass slide.

Following the vector diffraction theory of Richards and Wolf [1s], if a PW linearly polarized in the x direction is normally incident upon the system shown by Fig. S8, the electric field at a given point $\mathbf{r}$ in the focal region can be expressed as

$$E_x^x = -iA[I_0 + I_2\cos(2\phi)],$$
$$E_y^x = -iAI_2\sin(2\phi),$$
$$E_z^x = -2AI_1\cos(\phi),$$

(1)

where ϕ is the azimuthal angle of the point $\mathbf{r}$. $A = kfl_0/2$ is a constant proportional to the incident field amplitude l_0. The integrals I_n are defined by

$$I_0 = \int_0^\alpha \sqrt{\cos\theta_p}\sin\theta_p(1+\cos\theta_p)J_0(kr_p\sin\theta\sin\theta_p)\exp(ikr_p\cos\theta\cos\theta_p)d\theta_p,$$

$$I_1 = \int_0^\alpha \sqrt{\cos\theta_p}\sin^2\theta_p J_1(kr_p\sin\theta\sin\theta_p)\exp(ikr_p\cos\theta\cos\theta_p)d\theta_p,$$

(2)

$$I_2 = \int_0^\alpha \sqrt{\cos\theta_p}\sin\theta_p(1-\cos\theta_p)J_2(kr_p\sin\theta\sin\theta_p)\exp(ikr_p\cos\theta\cos\theta_p)d\theta_p,$$

where k is the magnitude of the wave vector of the fundamental beam. J_n is the Bessel function of the first kind with order n. θ is the polar angle of the point $\mathbf{r}$.

An analytical integral representation to calculate the field gradient of focused fields can be derived by using the differential recursion formula between the Bessel functions of different orders [2s]. For a PW linearly polarized in the x-direction, the electrical field gradient in the focal region can be expressed as [3s]

$$
\nabla\mathbf{E}^x =
\begin{vmatrix}
\dfrac{\partial E_x^x}{\partial x} & \dfrac{\partial E_y^x}{\partial x} & \dfrac{\partial E_z^x}{\partial x} \\[2mm]
\dfrac{\partial E_x^x}{\partial y} & \dfrac{\partial E_y^x}{\partial y} & \dfrac{\partial E_z^x}{\partial y} \\[2mm]
\dfrac{\partial E_x^x}{\partial z} & \dfrac{\partial E_y^x}{\partial z} & \dfrac{\partial E_z^x}{\partial z}
\end{vmatrix}
$$

(3)

$$
= -Ak
\begin{bmatrix}
i[\cos\phi(I_{-1}+I_1''\cos 2\phi)-\dfrac{2I_2\cos 3\phi}{kr\sin\theta}] & i(I_1''\cos\phi\sin 2\phi-\dfrac{2I_2\sin 3\phi}{kr\sin\theta}) & 2(I_0''\cos^2\phi-\dfrac{I_1\cos 2\phi}{kr\sin\theta}) \\[2mm]
i[\sin\phi(I_{-1}+I_1''\cos 2\phi)-\dfrac{2I_2\sin 3\phi}{kr\sin\theta}] & i(I_1''\sin\phi\sin 2\phi+\dfrac{2I_2\cos 3\phi}{kr\sin\theta}) & (I_0''\sin 2\phi-\dfrac{2I_1\sin 2\phi}{kr\sin\theta}) \\[2mm]
-(I_0'+I_2'\cos 2\phi) & -I_2'\sin 2\phi & i2I_1'\cos\phi
\end{bmatrix}
$$

The integrals I_n are related to the Bessel function and can be written as

$$I_{-1} = \int_0^\alpha \cos^{1/2}\theta_p \sin^2\theta_p (1+\cos\theta_p) J_{-1}(kr\sin\theta\sin\theta_p)\exp(ikr\cos\theta\cos\theta_p)\,\mathrm{d}\theta_p$$

$$I_0' = \int_0^\alpha \cos^{1/2}\theta_p \sin\theta_p (1+\cos\theta_p)\cos\theta_p J_0(kr\sin\theta\sin\theta_p)\exp(ikr\cos\theta\cos\theta_p)\,\mathrm{d}\theta_p$$

$$I_0'' = \int_0^\alpha \cos^{1/2}\theta_p \sin^3\theta_p J_0(kr\sin\theta\sin\theta_p)\exp(ikr\cos\theta\cos\theta_p)\,\mathrm{d}\theta_p$$

$$I_1' = \int_0^\alpha \cos^{3/2}\theta_p \sin^2\theta_p J_1(kr\sin\theta\sin\theta_p)\exp(ikr\cos\theta\cos\theta_p)\,\mathrm{d}\theta_p$$

$$I_1'' = \int_0^\alpha \cos^{1/2}\theta_p \sin^2\theta_p (1-\cos\theta_p) J_1(kr\sin\theta\sin\theta_p)\exp(ikr\cos\theta\cos\theta_p)\,\mathrm{d}\theta_p$$

$$I_2' = \int_0^\alpha \cos^{3/2}\theta_p \sin\theta_p (1-\cos\theta_p) J_2(kr\sin\theta\sin\theta_p)\exp(ikr\cos\theta\cos\theta_p)\,\mathrm{d}\theta_p$$

(4)

Following the same procedure, for a PW linearly polarized in the y-direction, the electric field and the corresponding field gradient are shown by

$$E_x^y = -iAI_2\sin(2\phi),$$
$$E_y^y = -iA[I_0 - I_2\cos(2\phi)],$$
$$E_z^y = -2AI_1\sin(\phi),$$

(5)

$$\nabla \mathbf{E}^y = \begin{vmatrix} \dfrac{\partial E_x^y}{\partial x} & \dfrac{\partial E_y^y}{\partial x} & \dfrac{\partial E_z^y}{\partial x} \\[2mm] \dfrac{\partial E_x^y}{\partial y} & \dfrac{\partial E_y^y}{\partial y} & \dfrac{\partial E_z^y}{\partial y} \\[2mm] \dfrac{\partial E_x^y}{\partial z} & \dfrac{\partial E_y^y}{\partial z} & \dfrac{\partial E_z^y}{\partial z} \end{vmatrix}$$

(6)

$$= -Ak \begin{bmatrix} i(I_1''\cos\phi\sin2\phi - \dfrac{2I_2\sin3\phi}{kr\sin\theta}) & i[\cos\phi(I_{-1}-I_1''\cos2\phi)+\dfrac{2I_2\cos3\phi}{kr\sin\theta}] & (I_0''\sin2\phi - \dfrac{2I_1\sin2\phi}{kr\sin\theta}) \\[3mm] i(I_1''\sin\phi\sin2\phi + \dfrac{2I_2\cos3\phi}{kr\sin\theta}) & i[\sin\phi(I_{-1}-I_1''\cos2\phi)+\dfrac{2I_2\sin3\phi}{kr\sin\theta}] & 2(I_0''\sin^2\phi + \dfrac{I_1\cos2\phi}{kr\sin\theta}) \\[3mm] -I_2'\sin2\phi & -(I_0'-I_2'\cos2\phi) & i2I_1'\sin\phi \end{bmatrix}$$

By rotating the quarter-wave plate in the experimental setup, the polarization state of the incident PW can be changed progressively from linear to circular. Elliptically or circularly polarized beams can be regarded as the linear superposition of linearly polarized beams in the x- and y-direction. The electrical field and corresponding field gradient are shown by

$$\mathbf{E}^{(\omega)}(\mathbf{r}) = [\exp(-\frac{i\varphi_2}{2})\cos^2\varphi_1 + \exp(\frac{i\varphi_2}{2})\sin^2\varphi_1]\mathbf{E}^x - 2i\sin(\frac{\varphi_2}{2})\sin\varphi_1\cos\varphi_1\mathbf{E}^y$$

$$\nabla\mathbf{E}^{(\omega)}(\mathbf{r}) = [\exp(-\frac{i\varphi_2}{2})\cos^2\varphi_1 + \exp(\frac{i\varphi_2}{2})\sin^2\varphi_1]\nabla\mathbf{E}^x - 2i\sin(\frac{\varphi_2}{2})\sin\varphi_1\cos\varphi_1\nabla\mathbf{E}^y$$

(7)

φ_1 and φ_2 are the polarization direction of the incident linearly polarized beam with respect to the optical axis of the wave plate and the phase delay of the wave plate, respectively. For a quarter-wave plate, $\varphi_2 = 90\,^\circ$.

In the Cartesian coordinate, bulk nonlinear polarization can be rewritten as

$$P_{bulk,x}^{(2\omega)}(\mathbf{r}) = 2\gamma \left(E_x^{(\omega)} \frac{\partial E_x^{(\omega)}}{\partial x} + E_y^{(\omega)} \frac{\partial E_y^{(\omega)}}{\partial x} + E_z^{(\omega)} \frac{\partial E_z^{(\omega)}}{\partial x} \right) + \delta' \left(E_x^{(\omega)} \frac{\partial E_x^{(\omega)}}{\partial x} + E_y^{(\omega)} \frac{\partial E_x^{(\omega)}}{\partial y} + E_z^{(\omega)} \frac{\partial E_x^{(\omega)}}{\partial z} \right),$$

$$P_{bulk,y}^{(2\omega)}(\mathbf{r}) = 2\gamma \left(E_x^{(\omega)} \frac{\partial E_x^{(\omega)}}{\partial y} + E_y^{(\omega)} \frac{\partial E_y^{(\omega)}}{\partial y} + E_z^{(\omega)} \frac{\partial E_z^{(\omega)}}{\partial y} \right) + \delta' \left(E_x^{(\omega)} \frac{\partial E_y^{(\omega)}}{\partial x} + E_y^{(\omega)} \frac{\partial E_y^{(\omega)}}{\partial y} + E_z^{(\omega)} \frac{\partial E_y^{(\omega)}}{\partial z} \right), \quad (8)$$

$$P_{bulk,z}^{(2\omega)}(\mathbf{r}) = 2\gamma \left(E_x^{(\omega)} \frac{\partial E_x^{(\omega)}}{\partial z} + E_y^{(\omega)} \frac{\partial E_y^{(\omega)}}{\partial z} + E_z^{(\omega)} \frac{\partial E_z^{(\omega)}}{\partial z} \right) + \delta' \left(E_x^{(\omega)} \frac{\partial E_z^{(\omega)}}{\partial x} + E_y^{(\omega)} \frac{\partial E_z^{(\omega)}}{\partial y} + E_z^{(\omega)} \frac{\partial E_z^{(\omega)}}{\partial z} \right).$$

The propagation of the SH field in a homogeneous and isotropic medium is governed by the inhomogeneous wave equation. The Green's function approach can be utilized to resolve the inhomogeneous wave equation. For far-field radiation ($\mathbf{R} \gg \mathbf{r}$), the SH radiation can be presented in spherical coordinates [4s,5s]:

$$\mathbf{E}^{(2\omega)}(\mathbf{R}) = \frac{\mu_0 \omega^2 \exp(i2kR)}{\pi R} \iiint\limits_{V} dV \exp(\frac{-i2k\mathbf{R}\cdot\mathbf{r}}{R})$$

$$\begin{bmatrix} 0 & 0 & 0 \\ \cos\Theta\cos\Phi & \cos\Theta\sin\Phi & -\sin\Theta \\ -\sin\Phi & \cos\Phi & 0 \end{bmatrix} \begin{bmatrix} P_{bulk,x}^{(2\omega)}(\mathbf{r}) \\ P_{bulk,y}^{(2\omega)}(\mathbf{r}) \\ P_{bulk,z}^{(2\omega)}(\mathbf{r}) \end{bmatrix}. \quad (9)$$

Here, Θ and Φ are the polar and azimuthal angles of the detection point $\mathbf{R}$, respectively.
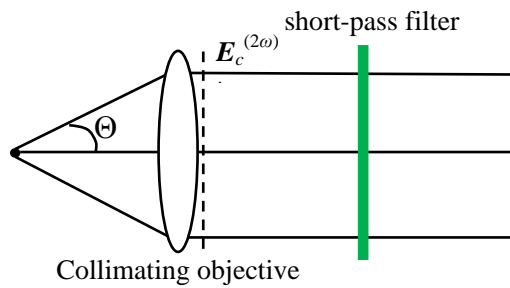

Fig. S9. Schematic of the detecting optical path.

The evolution of the SH signal through the collimating objective is illustrated by Fig.S9 and can be modeled by the generalized Jones matrix formalism. Following the Török's method [6s, 7s], the electric vector of the SH signal behind the collimating objective is given by

$$\mathbf{E}_c^{(2\omega)} = \frac{1}{A(\Theta)} R^{-1} \cdot L^{-1} \cdot R \cdot \mathbf{E}^{(2\omega)}(\mathbf{R}) \quad (10)$$

When the collimating objective obeys Abbe's sine condition, the apodization function A(θ) takes the form of $\cos^{1/2}\Theta$. The matrix R describes the coordinate transformation for rotation around the z axis and the matrix L describes the change in the electric field as it traverses the lens [6s, 7s]. On performing the matrix operations of Eq. (10), the electric field components in the Cartesian coordinate system are represented as

$$E_{c,x}^{(2\omega)} = \cos^{-1/2}\Theta\{-(\sin^2\Phi+\cos^2\Phi\cos\Theta)\,\mathrm{B}_x-[\sin\Phi\cos\Phi(\cos\Theta-1)]\,\mathrm{B}_y+\cos\Phi\sin\Theta\,\mathrm{B}_z\}$$
$$E_{c,y}^{(2\omega)} = \cos^{-1/2}\Theta\{-[\sin\Phi\cos\Phi(\cos\Theta-1)]\,\mathrm{B}_x-(\sin^2\Phi\cos\Theta+\cos^2\Phi)\,\mathrm{B}_y+\sin\Phi\sin\Theta\,\mathrm{B}_z\} \quad (11)$$
$$E_{c,z}^{(2\omega)} = 0$$

where

$$B_x = \frac{\mu_0\omega^2\exp(2\mathrm{i}kR)}{\pi R}\iiint\limits_V dV\exp(\frac{-i2k\boldsymbol{R}\cdot\boldsymbol{r}}{R})P_{bulk,x}^{(2\omega)}$$

$$B_y = \frac{\mu_0\omega^2\exp(2\mathrm{i}kR)}{\pi R}\iiint\limits_V dV\exp(\frac{-i2k\boldsymbol{R}\cdot\boldsymbol{r}}{R})P_{bulk,y}^{(2\omega)} \quad (12)$$

$$B_z = \frac{\mu_0\omega^2\exp(2\mathrm{i}kR)}{\pi R}\iiint\limits_V dV\exp(\frac{-i2k\boldsymbol{R}\cdot\boldsymbol{r}}{R})P_{bulk,z}^{(2\omega)}$$

6. Numerical simulations

6.1 The properties of the focused field

Fig. S10 gives the normalized intensity distribution of the focused field at *xy* and *xz* planes, respectively, when a PW linearly polarized in the x-direction is focused by an infinity-corrected objective. From Fig. S10, it can be found that the transverse and axial lengths of the focused field are approximately 1.0 μm and 3.0 μm, respectively. The intensity distributions of the $\nabla\mathbf{E}^x$ components are shown by Fig. S11, which are normalized with respect to the maximum of $\nabla\mathbf{E}^x$. According to Figs. S10 and S11, the focused field is highly localized in the z-direction compared to the thickness of glass slides.
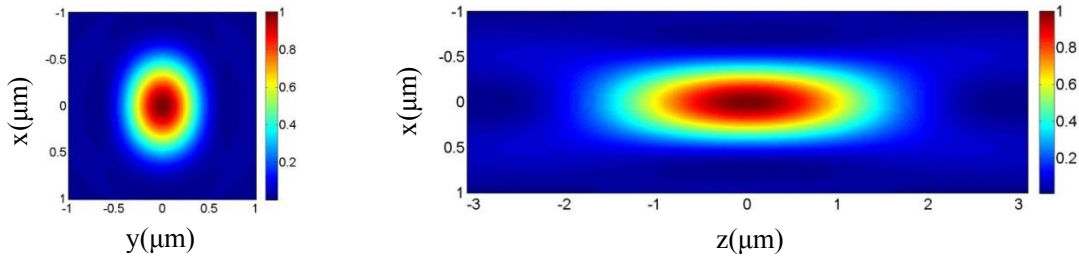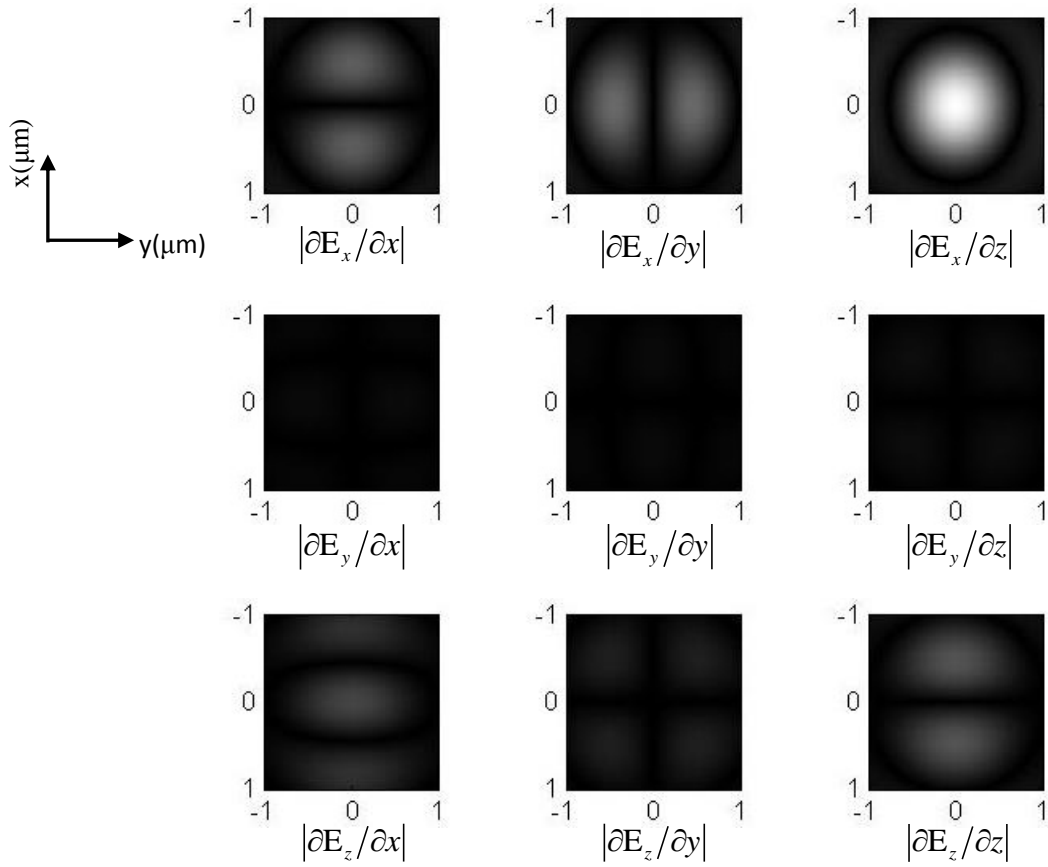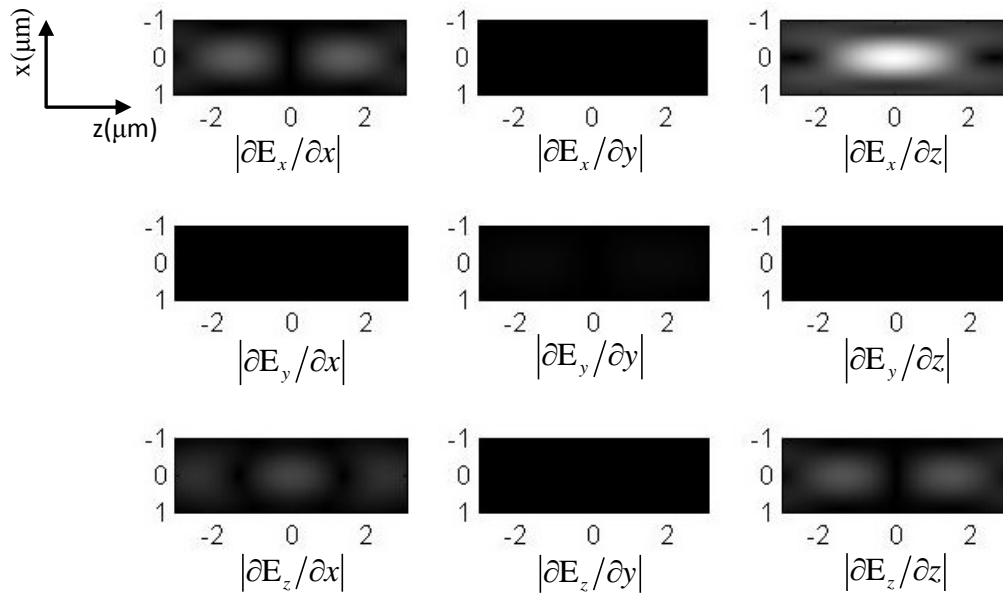

Fig. S10. Normalized intensity distribution of the focused field $\mathbf{E}^x$ on the *xy* (a) and *xz* (b) planes, respectively. NA=0.85, λ=1075nm.

x(μm)

y(μm)

$|\partial E_x/\partial x|$

$|\partial E_x/\partial y|$

$|\partial E_x/\partial z|$

$|\partial E_y/\partial x|$

$|\partial E_y/\partial y|$

$|\partial E_y/\partial z|$

$|\partial E_z/\partial x|$

$|\partial E_z/\partial y|$

$|\partial E_z/\partial z|$

(a)

x(μm)

z(μm)

$|\partial E_x/\partial x|$

$|\partial E_x/\partial y|$

$|\partial E_x/\partial z|$

$|\partial E_y/\partial x|$

$|\partial E_y/\partial y|$

$|\partial E_y/\partial z|$

$|\partial E_z/\partial x|$

$|\partial E_z/\partial y|$

$|\partial E_z/\partial z|$

(b)

Fig. S11 Normalized intensity distributions of $\nabla \mathbf{E}^x$ components on the *xy* (a) and *xz* (b) planes, respectively. NA=0.85, λ=1075nm.

The NA of the focusing objective plays a crucial role in creating the field gradient. The magnitude of field gradient in the focal region will greatly decrease when NA is low, as shown in Fig. S12. This explains why there is no noticeable bulk SHG in the previously reported experiment, where although a glass slide was excited by the focused field, the NA of the focusing objective might not be sufficiently high.
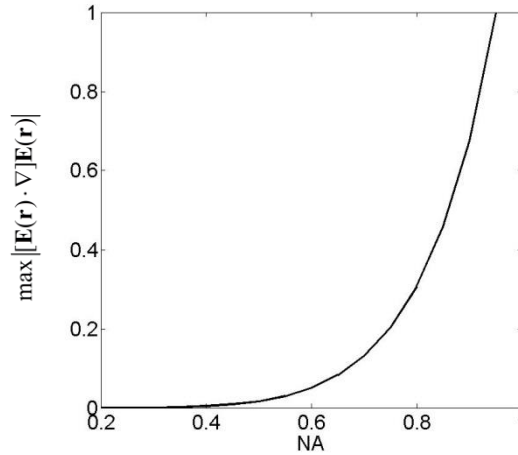

Fig. S12 Variation of $\max\left|[\mathbf{E}(\mathbf{r})\cdot\nabla]\mathbf{E}(\mathbf{r})\right|$ with NA.

6.2 Bulk SHG by the transverse field gradient perpendicular to the beam propagation direction
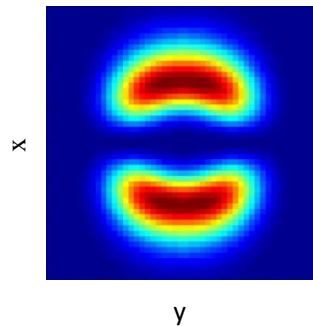

Fig. S13 Radiation pattern of SHG inside glass slide when the components in the longitudinal z-direction are ignored.

In some previously published papers, the radiation pattern of SH exhibits a two-lobe structure while the orientation of those two lobes is parallel to the x-direction, for a PW linearly polarized in the x-direction. This orientation is 90-degree apart from our results. The reason is that the previously reported SHG in [17,26] were predominately resulting from the transverse field gradient with negligible components in the longitudinal z-direction. Indeed in the numerical modeling, by setting the field component in the longitudinal z-direction to zero, the radiation pattern of SH would rotate 90-degree, as given by Fig. S13, which agrees with the observations in [17, 26].

REFERENCES

[1s] B. Richards, and E. Wolf, Electromagnetic diffraction in optical systems II. Structure of the image field in an aplanatic system, Proc. Roy. Soc. A **253**, 358 (1959).

[2s] G. B. Arfken, and H. J. Weber, "Bessel functions," in Mathematical Methods for Physicists (Academic, 2005) p. 678-739.

[3s] B. Z. Huo, X. H. Wang, S. J. Chang, M. Zeng, and G. H. Zhao, Second harmonic generation of individual centrosymmetric sphere excited by a tightly focused beam, J. Opt. Soc. Am. B **28**, 2702 (2011).

[4s] J. X. Cheng, Andreas Volkmer, and X. S. Xie, Theoretical and experimental characterization of coherent anti-Stokes Raman scattering microscopy, J. Opt. Soc. Am. B **19**, 1363 (2002).

[5s] J. X. Cheng, and X. S. Xie, Coherent Anti-Stokes Raman Scattering Microscopy: Instrumentation, Theory, and Applications, J. Phys. Chem. B **108**, 827 (2004).

[6s] P. Török, P. D. Higdon, and T. Wilson, Theory for confocal and conventional microscopes imaging small dielectric scatterers, J. Mod. Opt. **45**, 1681 (1998).

[7s] O. Haeberlé, M. Ammar, H. Furukawa, K. Tenjimbayashi, and P. Török, Point spread function of optical microscopes imaging through stratified media, Opt. Express **11**, 2964 (2003).